Hybrid Modulation PWM-Controlled Multifrequency and Multiload WPT System Based on Variable Resonant Network

Chenyang Xia, *Member, IEEE*, Yunhai Liu, Chenxu Wang, Zijian Yang, Gang Ren, Jiaan Yan, Hao Lu, Anran Sun, and Yang Lu

***Abstract*—In order to reduce the reactive power of the existing hybrid modulation pulsewidth modulation (HM-PWM)-controlled multifrequency and multiload wireless power transfer (MFML WPT) system without a resonant network, a design idea of a variable resonant network is proposed, accordingly, an HM-PWM-controlled MFML WPT system based on a variable resonant network is studied. According to the variation in load frequency, the output frequency of the inverter and the frequency of the variable resonant network can change accordingly. First, the structure and working principle of the MFML WPT system based on a variable resonant network are introduced. Second, taking a dual-frequency variable resonant network as an example, the control method and range of frequency adjustment are studied by modeling. Third, the MFML WPT system based on a variable resonant network is mathematically modeled, the output power and efficiency are analyzed. Finally, the feasibility of the design idea of the variable resonant network is proved by experiments. The results show that in the range of 20–90 kHz, the variable resonant network can realize stable switching of any two frequencies, and the power factor of the system can reach 0.99. So, the MFML WPT system can realize high-efficiency WPT for loads with different frequencies.**

***Index Terms*—Hybrid modulation pulsewidth modulation (HM-PWM) control, multifrequency, multiload, variable resonant network, wireless power transfer (WPT).**

I. Introduction

WIRELESS power transfer (WPT) technology is a new energy transmission technology based on space soft media to achieve clean, safe, flexible, and efficient use of energy [1], [2], [3]. It has been widely used in electric vehicles [4], aerospace [5], smart grid [6], new energy power generation [7], medical equipment [8], and communication equipment [9].

In recent years, with the development and popularization of WPT technology, the application of WPT system has gradually expanded from single-frequency and single-load power supply modes to multifrequency and multiload (MFML) power supply modes. For MFML WPT system, the current research mainly focuses on the multifrequency power generation mode and the multifrequency resonant network structure design of a MFML WPT system.

For the research of the multifrequency power generation mode of an MFML WPT system, the current methods mainly include the following.

1) Utilizing multiple inverters with different frequencies connected in parallel to obtain multifrequency power [10]. For example, multiple inverters are connected in parallel in [10] to realize the output of multifrequency electric energy.
2) Utilizing the harmonic characteristics of the inverter to obtain multifrequency power [11], [12]. For example, Liu et al. [11] proposed a new inverter structure, adding two diodes to the traditional inverter structure so that the inverter can output multifrequency power. Qi et al. [12] used the fundamental wave and harmonics output by the inverter to transmit multifrequency power.
3) Utilizing a special modulation mode to control the inverter to obtain multifrequency power [13], [14]. For example, Han et al. [13] obtained the control signal of the inverter through calculation, then used the signal to control the inverter, so as to realize the multifrequency power output of the inverter. Ye et al. [14] proposed the pulse density modulation method to control the inverter, so as to realize the multifrequency power output.

Through the comparison and analysis, it can be found that, compared with the former two methods, the third method is gradually studied in depth due to the advantages of adjustable inverter output frequency.

For the research of an MFML WPT system, the current research mainly focuses on the following.

1) The design of a multifrequency resonant network with fixed frequencies [12]. For example, Qi et al. [12] studied the parameter design method of the base Cole network and

Manuscript received 22 September 2023; revised 15 November 2023; accepted 7 December 2023. Date of publication 21 December 2023; date of current version 26 January 2024. This work was supported in part by the National Natural Science Foundation of China under Grant 52277020 and in part by the Natural Science Foundation of Jiangsu Province under Grant BK20211246. Recommended for publication by Associate Editor J. Acero. *(Corresponding author: Chenyang Xia.)*

The authors are with the Jiangsu Province Laboratory of Mining Electric and Automation, China University of Mining and Technology, Xuzhou 221008, China (e-mail: chyxia@cumt.edu.cn; liuyunhaicumt@163.com; ts23230043-a31ld@cumt.edu.cn; yangzijian@cumt.edu.cn; rengang@cumt.edu.cn; ts2113-0084a31ld@cumt.edu.cn; ts21130168p31@cumt.edu.cn; tb21130007b2@cumt.edu.cn; luyang52121@cumt.edu.cn).

Color versions of one or more figures in this article are available at https://doi.org/10.1109/TPEL.2023.3345351.

Digital Object Identifier 10.1109/TPEL.2023.3345351

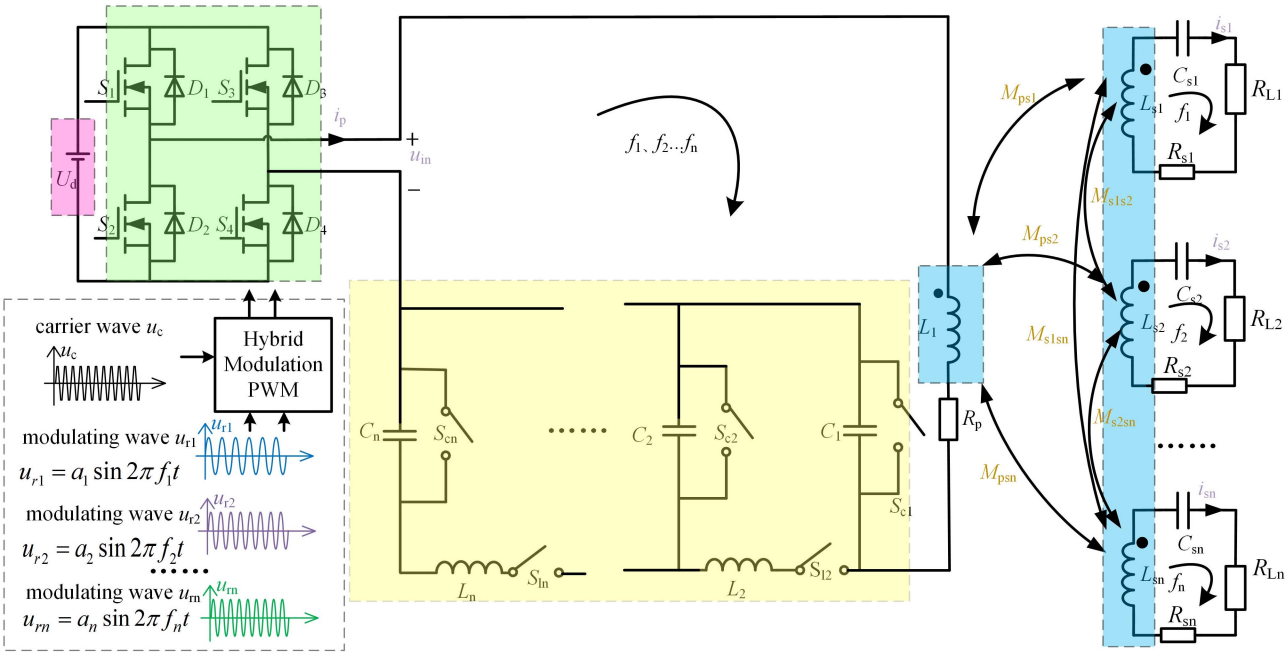

Fig. 1. Multifrequency and multiload WPT system based on variable resonant network controlled by HM-PWM.

the Foster network, which made the parameter calculation of a resonant network with multiple different frequencies easier.

2) Multifrequency resonant network with adjusted frequencies [15], [16]. For example, Abramov and Peretz [15] designed variable inductors based on the transformer model, so as to form a variable resonant network. The transformer model controls the variation of the inductance value in the circuit, so as to change the resonant frequencies of the resonant network. Saltanovs [16] used a capacitor matrix and changed the resonant frequencies of the resonant network by controlling the capacitor value of the capacitor matrix to access the circuit.

Through the comparison and analysis, it can be found that, compared with the former method, the second method has been widely studied and applied in the WPT system because its resonant frequencies are variable.

In the previous work of the researchers in this article, an MFML WPT system using hybrid modulation pulsewidth modulation (HM-PWM) control method is proposed [17], it shows that the MFML WPT system controlled by HM-PWM can realize independent and controllable wireless power supply for loads with different frequencies and power levels. However, due to the zero compensation strategy, the reactive power of the primary side is abundant, the power factor and the efficiency of the system are quite low. Therefore, in view of the above shortcomings, this article proposes a design idea of introducing variable elements into multifrequency resonant network. In order to verify the feasibility of this idea, a variable resonant network topology based on the basic topology is proposed. The topology is verified using an HM-PWM-controlled MFML WPT system. According to the requirement of multiload frequency, the output control of the primary multifrequency composite power supply is realized by changing the frequency of hybrid modulating wave. Through the control of the switching device of the variable resonant network, the frequency of the multiresonant network is changed. Finally, the flexible and efficient radio energy transmission of MFML under HM-PWM control mode is realized.

The rest of this article is organized as follows. Section II introduces the structure and working principle of HM-PWM-controlled MFML WPT system based on variable resonant network. In Section III, the variable resonant network is modeled, then the control method and adjustment range of the variable resonant network are analyzed. In Section IV, the MFML WPT system is modeled, then the power and efficiency characteristics of the system are analyzed. In Section V, experimental verification is carried out. Finally, Section VI concludes this article.

II. Structure and Working Principle of HM-PWM-Controlled MFML WPT System Based on Variable Resonant Network

The structure of an HM-PWM-controlled MFML WPT system based on a variable resonant network is shown in Fig. 1.

In Fig. 1, the HM-PWM-controlled MFML WPT system based on a variable resonant network includes dc power supply (U_d), high-frequency inverter circuit (S_1-S_4, D_1-D_4), primary variable resonant network (C_1-C_n, L_2-L_n, S_{c1}-S_{cn}, S_{l2}-S_{ln}), transmitting coil (L_1), MFML power receiving device (L_{s1}, C_{s1}, R_{L1}, L_{s2}, C_{s2}, R_{L2} ... L_{sn}, C_{sn}, R_{Ln}), and PWM control circuit. R_p is the equivalent internal resistance of the primary resonant network, and the secondary MFML power-receiving device comprises n receiving coils and n compensation capacitors, which constitute n resonant circuits, respectively. The natural resonant frequencies of the secondary receiving loop are $f_1, f_2, ... f_n$. Among them, L_{s1} and C_{s1} constitute the frequency

selection network of frequency f_1, and L_{s2} and C_{s2} constitute the frequency selection network of frequency f_2 ... L_{sn} and C_{sn} constitute the frequency selection network of frequency f_n.

The output terminals of different resonant networks are connected to the loads R_{L1}, R_{L2} ... R_{Ln}. M_{ps1}, M_{ps2} ... M_{psn} are the mutual inductors between the transmitting coil and each receiving coil. M_{s1s2}, M_{s1sn}, M_{s2sn} ... are cross-inductance between different receiving coils.

The primary variable resonant network (C_1-C_n, L_2-L_n, S_{c1}-S_{cn}, S_{l2}-S_{ln}) can change the equivalent value of each component(C_1-C_n, L_2-L_n) by controlling the switch (S_{c1}-S_{cn}, S_{l2}-S_{ln}), so as to change the resonant frequency of the resonant network.

In order to minimize the impact of cross-inductance, a parameter design principle was proposed in the previous research work [17]. In the previous research of the author of this article, through theoretical analysis and experimental verification, a parameter design criterion is proposed, which can reduce the cross-inductance of the secondary sides [17]. The experimental results show that the cross inductance between the secondary sides can be ignored when the parameters are designed according to the criterion. Therefore, cross-inductance is not considered in the subsequent research of this article. At the same time, the design principles of frequency selective network parameters are shown in the following:

$$\begin{cases} (2\pi f_1)^2 = \frac{1}{L_{s1}C_{s1}} \\ (2\pi f_2)^2 = \frac{1}{L_{s2}C_{s2}} \\ \cdots\cdots \\ (2\pi f_n)^2 = \frac{1}{L_{sn}C_{sn}} \end{cases}. \tag{1}$$

According to the previous research, the inverter of the MFML WPT system based on variable resonant network adopts HM-PWM control mode.

The carrier of the HM-PWM control circuit is the triangular wave u_c, and the modulated wave adopts the hybrid modulated wave u_r which is superimposed by multiple sinusoidal waves with adjustable frequency. Hybrid modulated wave u_r is

$$\begin{aligned} u_r &= u_{r1} + u_{r2} + \ldots + u_{rn} \\ &= a_1 \sin 2\pi f_1 t + a_2 \sin 2\pi f_2 t + \ldots + a_n \sin 2\pi f_n t \end{aligned} \tag{2}$$

where a_1, a_2, ... a_n are the modulation amplitudes of each frequency.

In order to avoid overmodulation, the HM-PWM-controlled inverter is kept within the effective PWM operating range, and the amplitude of the hybrid modulated wave does not exceed the carrier amplitude. In addition, the switching frequency of the inverter is consistent with the carrier frequency f_c, and the frequency f_r of the modulated wave is equal to the ratio of the carrier frequency f_c to the modulation ratio N(f_r=f_c/N). Based on the transmission frequencies f_1, f_2, ... f_n, set the carrier frequency to the least common multiple of the transmission frequency. Therefore, ensure that the carrier ratio N is an integer to avoid additional harmonic interference. According to the requirements of switching frequency and carrier ratio of inverter, the upper limit of modulating wave frequency can be determined.

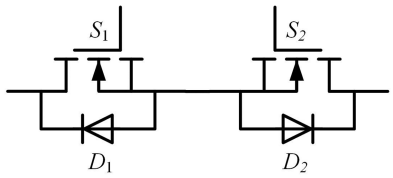

Fig. 2. Bidirectional switch structure.

Based on this, the control principle of the HM-PWM-controlled MFML WPT system inverter is as follows [17]: according to different loads R_{L1}, R_{L2}, ... R_{Ln}, set the modulated wave signal of corresponding frequency f_1, f_2, ... f_n. According to the power requirements of different loads, the amplitudes of different frequency modulated waves a_1, a_2, ... a_n are designed. The basic modulation method is to superposition the modulated waves of different frequencies f_1, f_2, ... f_n and amplitudes a_1, a_2, ... a_n to obtain the hybrid modulated wave signal u_r, and the inverse signal is -u_r.

The signal modulated by hybrid modulated wave u_r and u_c triangular carrier is used as the driving signal of the front axle arm, while the signal modulated by composite modulated wave -u_r and triangular carrier u_c is used as the driving signal of the rear axle arm. Accordingly, the high-frequency inverter will output high-frequency hybrid pulse waves containing different load frequencies.

In Fig. 1, the HM-PWM-controlled MFML WPT system adopts a variable resonant network with *n* switch controlled capacitor (SCC) components (S_{c1}-S_{cn}, C_1-C_n) and *n*-1 switch controlled inductance (SCI) (S_{l2}-S_{ln}, L_2-L_n). In Fig. 2, each SCC consists of a tuned capacitor and a bidirectional switch in parallel. Each SCI consists of a tuned inductor and a bidirectional switch in series. The bidirectional switch is composed of two MOSFETs in series in reverse.

In order to reduce reactive power and improve transmission efficiency of HM-PWM controlled MFML WPT system, the working mode of the variable resonant network is as follows. 1) For single-frequency and single-load working mode, S_{l2}-S_{ln} and S_{c2}-S_{cn} are disconnected. Only S_{c1} is connected to the circuit. The resonant network has only one resonant frequency. By changing the control angle of S_{c1}, the equivalent capacitor value of C_1 can be changed, and the resonant frequency of the resonant network can be changed, so that the resonant frequency follows the load frequency. 2) For dual-frequency and dual-load working mode, S_{l3}-S_{ln} and S_{c3}-S_{cn} are disconnected. S_{c1}, S_{c2}, S_{l1} are connected to the circuit. The resonant network has two resonant frequencies. By changing the control angles of S_{c1}, S_{c2}, and S_{l1}, respectively, the equivalent values of C_1, C_2, and L_2 can be changed, thus, changing the resonant frequency of the resonant network and making the resonant frequency follow the load frequency.

Similarly, for MFML working mode, S_{c1}-S_{cn}, S_{l2}-S_{ln} are connected to the circuit. The resonant network has *n* resonant frequencies. By changing the control angle of S_{c1}-S_{cn}, S_{l2}-S_{ln} separately, can change the equivalent values of C_1-C_n, L_2-L_n, thus, changing the resonant frequency of the resonant network. Therefore, the dynamic transformation of the resonant network

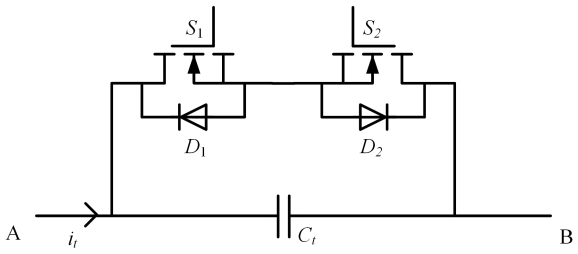

Fig. 3. Schematic diagram of SCC.

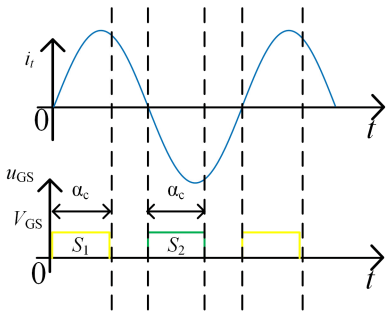

Fig. 4. Control angle of SCC.

is realized to ensure the efficient wireless power supply of MFML.

III. Variable Resonant Network Modeling and Control Method of MFML WPT System Based on HM-PWM Control

According to the analysis in Section II, when the load frequency changes, the dynamic change of the resonant frequency can be realized by controlling the change of the resonant network topology. And the output frequency of the inverter can follow the change. The key is to control the equivalent value of SCC and SCI accurately. The SCC and SCI equivalent circuits are analyzed below.

A. Equivalent Calculation of Switching Capacitor

The power electronic MOSFET switches S_1 and S_2 are connected in parallel at both ends of the capacitor C_t in reverse series, thus, forming a basic unit of SCC in Fig. 3 [18].

S_1 and D_2 constitute a forward transmission channel, while S_2 and D_1 constitute a reverse transmission channel. Among them, both D_1 and D_2 need to meet the requirements of high current and high frequency. Schottky diode with a low turn-ON voltage drop and high current needs to be selected. Since MOSFET and diode are connected in parallel across the capacitor, its voltage is resonance voltage, which is much larger than the input voltage of the system. Therefore, there is a high requirement for the withstand voltage level of MOSFET and diode. By controlling the control angle α_c of the two switching devices S_1 and S_2, the equivalent capacitor value of the SCC can be changed, and the specific control method is shown in Fig. 4.

In each period T = 2π, S_1 is switched ON in a positive half period, starting from time t = 0, and the switching time is $\alpha_c/2\pi$.

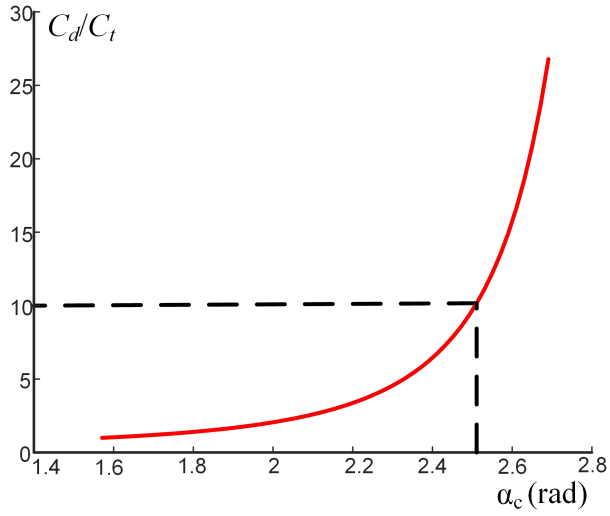

Fig. 5. Proportional relationship between the equivalent capacitor C_d and the actual capacitor C_t varies with the curve of α_c.

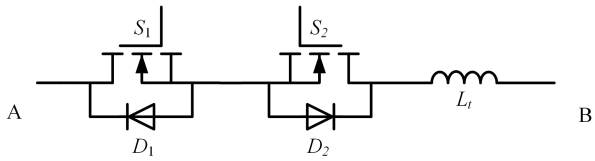

Fig. 6. Schematic diagram of SCI.

S_2 is switched ON in a negative half period, starting from time t = T/2, and the switching time is $\alpha_c/2\pi$, where $\alpha_c \in [\pi/2,\pi)$.

In this working mode, the equivalent capacitor C_d at both ends of A and B is [18]

$$C_d = \frac{C_t}{2-(2\alpha_c - \sin 2\alpha_c)/\pi}. \tag{3}$$

According to (3), when C_d/C_t is determined, the control angle α_c of the switching device can be solved.

In order to analyze the relationship between the equivalent capacitor C_d and α_c, based on (3), the relationship between the equivalent capacitor C_d, the actual capacitor C_t and α_c are analyzed and obtained in Fig. 5.

In Fig. 5, C_d/C_t increases with the increase of α_c and the slope of the curve gradually increases. When C_d/C_t <10, the curve rises gently, and the equivalent capacitor of the SCC in this section is less affected by the control error, also, the control difficulty is low. Therefore, it is selected to adjust the SCC within this range.

B. Equivalent Calculation of Switching Inductance

The power electronic MOSFET switches S_1 and S_2 are in series in reverse, and then in series with the inductor L_t to form a switching inductor basic unit in Fig. 6.

S_1 and D_2 constitute a forward channel, while S_2 and D_1 constitute a reverse channel. The equivalent inductance value of the switching inductance can be changed by controlling the

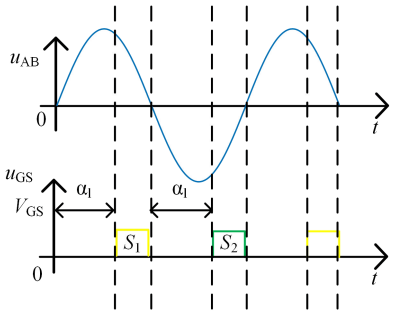

Fig. 7. Control angle of SCI.

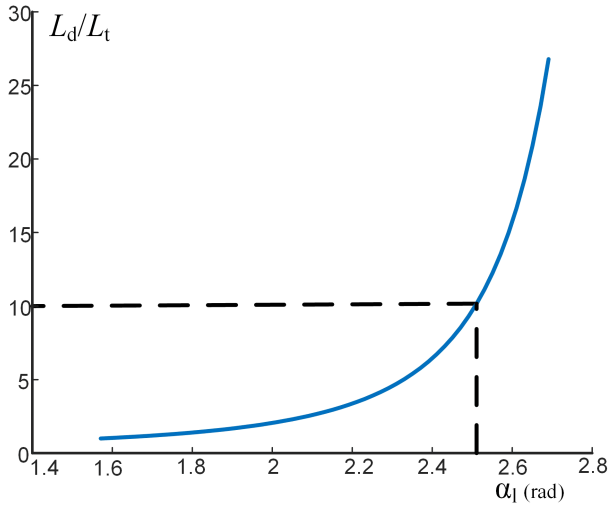

Fig. 8. Proportional relationship between the equivalent inductance L_d and the actual inductance L_t varies with α_l.

control angle α_l of the two switching devices S_1 and S_2. The specific control method is shown in Fig. 7.

In each period T $= 2\pi$, S_1 is switched ON in a positive half period, starting from time t $= \alpha_l/2\pi$, and the switching time is $\pi - \alpha_l/2\pi$. S_2 is switched ON in a negative half period, starting from time t = T/2 + $\alpha_l/2\pi$, and the switching time is $\pi - \alpha_l/2\pi$, where $\alpha_l \in [\pi/2, \pi)$.

In this working mode, the equivalent inductance L_d at both ends of A and B is [18]

$$L_d = \frac{L_t}{2 - (2\alpha_l - \sin 2\alpha_l)/\pi}. \tag{4}$$

According to (4), when L_d/L_t is determined, the control angle α_l of the switching device can be solved.

In order to analyze the relationship between the equivalent inductance L_d and α_l, based on (4), the relationship between the equivalent inductance L_d, the actual inductance L_t and α_l is analyzed and obtained in Fig. 8.

As can be seen from Fig. 8, L_d/L_t increases with the increase of α_l and the slope of the curve gradually increases. When L_d/L_t <10, the curve rises gently, and the equivalent inductance value of the SCI in this section is less affected by the control error, also, the control difficulty is low. Therefore, the SCI is adjusted in this range.

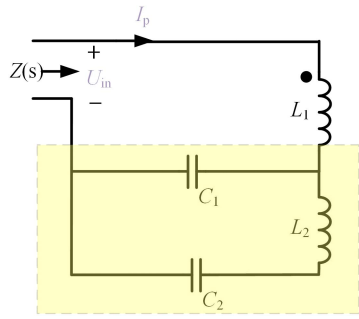

Fig. 9. Dual-frequency variable resonance network schematic diagram.

In Figs. 5 and 8, the curve in the figure can be roughly divided into two segments, one with a smaller slope and the other with a larger slope. Through the analysis in this article, it is known that when the slope is small, the error caused by the control has little influence on the equivalent value of the capacitor and inductance. Therefore, we choose to control section with a small slope of the curve. 10 of C_d/C_t <10 and L_d/L_t <10 is not unique and should be set according to the conditions of practical application. When the selected value is too large, although the adjustment range can be increased, the control precision will be higher. Therefore, this article chooses to study under the conditions of C_d/C_t and L_d/L_t <10.

C. Parameter Design of Multifrequency Resonant Network

The parameters of dual-frequency resonant network are analyzed. Based on the system shown in Fig. 1, a typical dual-frequency resonant network is designed in Fig. 9.

Based on Fig. 9, the equivalent impedance Z_s of the network can be obtained as follows:

$$Z(s) = sL_1 + \frac{1}{sC_1 + \frac{1}{sL_2 + \frac{1}{sC_2}}}. \tag{5}$$

Let $\omega = 2\pi f$, $s = j\omega$ and Z(s) = 0 [1], [2], under the conditions of known L_1, f_1, f_2, the expression of C_1, L_2, C_2 can be obtained as follows:

$$\begin{cases} C_1 = \frac{1}{4\pi^2 L_1 \left(f_1^2 - f_1 f_2 + f_2^2\right)} \\ L_2 = \frac{L_1 \left(f_1^2 - f_1 f_2 + f_2^2\right)^2}{f_1 (f_1 - f_2) f_2} \\ C_2 = \frac{(f_1 - f_2)^2}{4\pi^2 L_1 f_1 f_2 \left(f_1^2 - f_1 f_2 + f_2^2\right)}. \end{cases} \tag{6}$$

The purpose of an input impedance of 0 is to reduce the reactive power of the system. The efficiency of the system is improved by adding the compensation capacitor to offset the inductive reactive power generated by the inductance of the coil.

D. Modeling of Variable Resonant Network

Controlled by the HM-PWM and based on a variable resonant network, the MFML WPT system is shown in Fig. 1. Combined with the analysis of SCC, SCI, and the basic dual-frequency resonant network in Section III-A–C, the mathematical model of the dual-frequency resonant network is established. The actual circuit of the dual-frequency variable resonant network consists

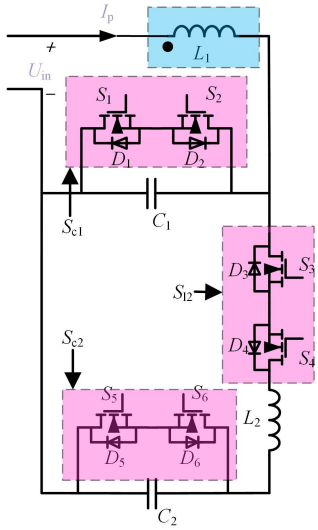

Fig. 10. Equivalent circuit diagram of dual-frequency resonant network.

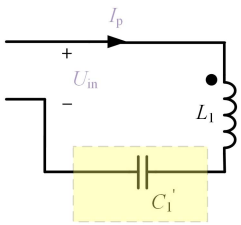

Fig. 11. Equivalent circuit diagram of variable resonant network operating in single-frequency mode.

of capacitors C_1 and C_2, inductor L_2, transmitting coil L_1, and switching devices S_1-S_6 in Fig. 10. The network can work in both single-frequency mode and dual-frequency mode.

According to the analysis in Section III-A–III-B, the control angle of the switching device can be determined when the ratio of the target value of the SCC and inductance to the initial value is determined. Therefore, the single-frequency and dual-frequency variable resonant networks are studied separately in order to determine the control angles of each switching device.

1) Single-Frequency Variable Resonant Network: When S_{c2} and S_{l2} are disconnected and S_{c1} is connected to the circuit, the variable resonant network works in single-frequency mode in Fig. 11.

It is assumed that the resonant frequency of the resonant network before frequency switching is f_1, the initial parameter of the resonant network is C_1, and the resonant frequency of the resonant network after frequency switching is f_1'. The expression of C_1 before switching is shown in the following [5]:

$$C_1 = \frac{1}{4\pi^2 f_1^2 L_1}. \tag{7}$$

After switching, the expression for C_1' is shown in the following:

$$C_1' = \frac{1}{4\pi^2 f_1'^2 L_1} \tag{8}$$

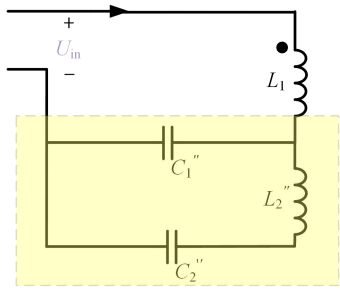

Fig. 12. Equivalent circuit diagram of variable resonant network operating in dual-frequency mode.

where C_1' is the equivalent capacitor of the SCC.

Let $f_1'/f_1 = \mathrm{a}$, based on (7) and (8), the relationship between C_1' and C_1 is shown in the following:

$$C_1' = \frac{1}{a} C_1. \tag{9}$$

By combining (3) and (9), the control angle α_{c1}' of S_{c1} can be obtained.

In practical application, when the load frequency changes from $f$to f', the controller can calculate the change α of the target capacitor through (9), and then the control angle α_c can be calculated by (3). The corresponding control signal is output to S_{c1} so that the value of C_1 is equivalent to C_1', thus the resonant frequency of the resonant network is switched.

2) Dual-Frequency Variable Resonant Network: When S_{c1}, S_{c2}, and S_{l2} are all connected to the circuit, the variable resonant network works in dual-frequency mode in Fig. 12.

It is assumed that the resonant frequency of the resonant network before frequency switching is f_1 and f_2, and the initial parameters of the resonant network are C_1, C_2, and L_2. After switching, the resonant frequency of the resonant network is f_1'' and f_2'', and the resonant network parameters are C_1'', C_2'', and L_2''. Substituting $f_1''/f_1 = \mathrm{a}$, $f_2''/f_2 = \mathrm{b}$, $f_2/f_1 = \mathrm{t}$ into (6), it can be obtained that

$$\begin{cases} C_1'' = \frac{1-t+t^2}{a^2-abt+b^2t} C_1 \\ L_2'' = \frac{\left(a^2-abt+b^2t^2\right)^2}{abt(a-bt)^2} \frac{t(1-t)^2}{(1-t+t^2)^2} L_2 \\ C_2'' = \frac{(a-bt)^2}{abt(a^2-ab+b^2t^2)} \frac{t\left(1-t+t^2\right)}{(1-t)^2} C_2 \end{cases} \tag{10}$$

where C_1'' and C_2'' are the equivalent capacitor of the SCC, and L_2'' is the equivalent inductance of the SCI.

The control angles α_{c1}'', α_{c2}'', α_{l2}'' of S_{c1}, S_{c2}, and S_{l2} can be obtained by combining (3) and (4).

The above is the analysis of a dual-frequency variable resonant network, and its analysis method can be extended to a multifrequency variable resonant network.

3) Multifrequency Variable Resonant Network: When the number of resonant frequencies is m (m =1.2 ... n) in the circuit, C_1-C_m.L_1-L_m is connected to the circuit to adjust the resonant frequency. At this time, the other n-m capacitors and n-m inductors are not connected to the circuit.

One of the innovations of this article is to put forward the idea of introducing variable elements into a multifrequency resonant

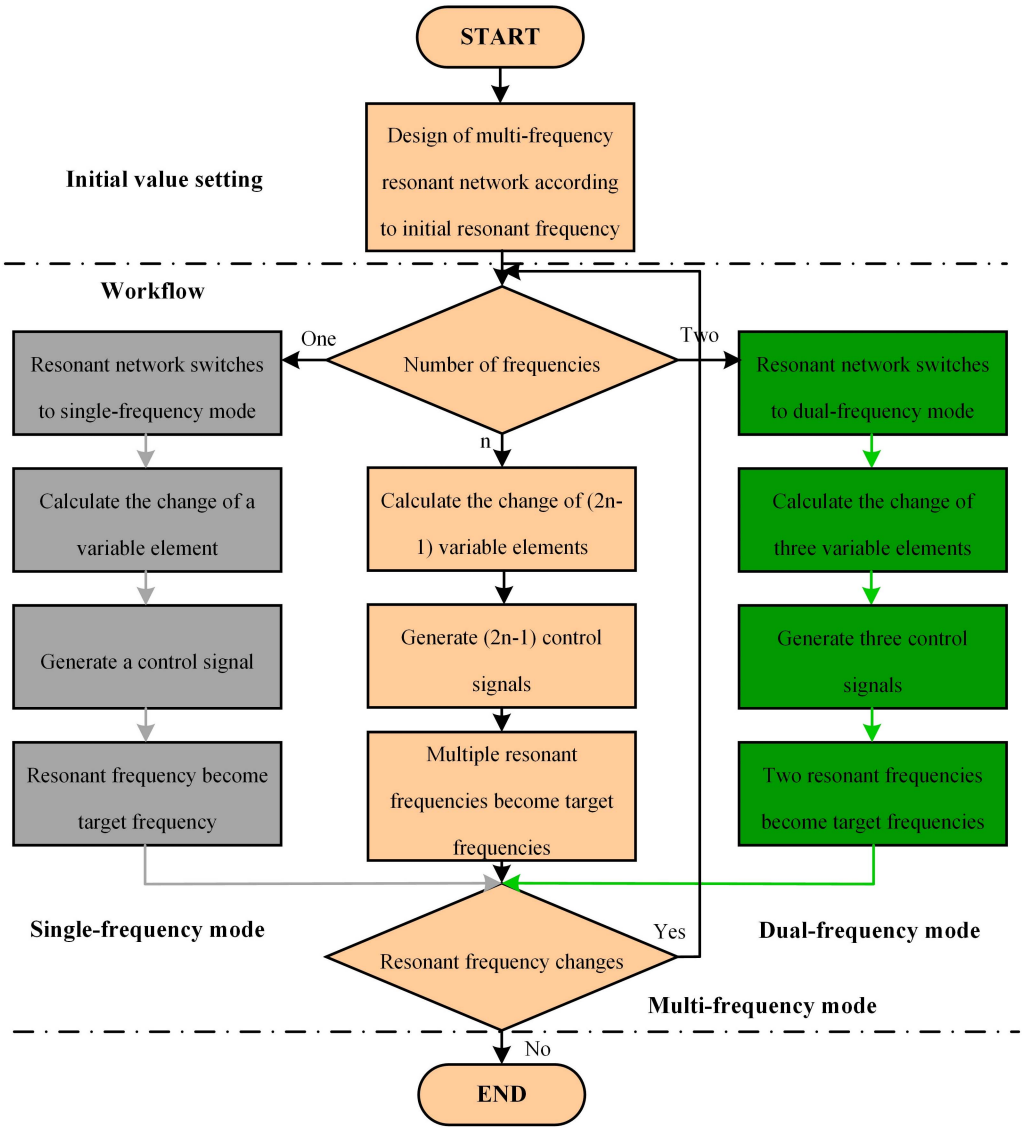

Fig. 13. Variable resonance network parameter design and adjustment flowchart.

network to construct a variable resonant network. In fact, the multifrequency situation is similar to the dual-frequency case, except that the number of variable devices is increased, and the control mode is consistent with the dual-frequency case. Therefore, the research and analysis methods in this article can be directly extended to the multifrequency case.

E. Variable Resonant Network Resonant Frequency Adjustment Method

As can be seen from Fig. 5, when C_d/C_t <10, the curve rises gently, and the equivalent capacitor in this section is less affected by the control error, and the control difficulty is also low. Therefore, the SCC is adjusted within this range.

In Fig. 11, in the case of a single-frequency resonant network, after the capacitor C_1 is connected to the switching device, its equivalent value varies in the range $[C_1, 10C_1]$. According to (7), when the initial frequency is f_1, the adjustment range in the resonant frequency can be obtained as $[0.316f_1, f_1]$.

In Fig. 12, in the case of a dual-frequency resonant network, the resonant frequencies f_1 and f_2 are determined by L_1, L_2, C_1, and C_2. Since the transmitting coil cannot be changed, the resonant frequency change in the variable resonant network is determined by L_2, C_1, and C_2. This problem is transformed into the range of two ternary functions. It is difficult to solve this problem directly, so in order to simplify the analysis and determine the resonant variation range of the dual-frequency variable resonant network, $f_1''/f_1 = f_2''/f_2 = \mathrm{a}$, $f_2/f_1 = \mathrm{t}$, f_1 and f_2 are the initial values of the resonant frequency of the resonant network, f_1'' and f_2'' are the target values of the resonant frequency, then (10) can be simplified to

$$\begin{cases} C_1'' = \frac{1}{a^2} C_1 \\ L_2'' = L_2 \\ C_2'' = \frac{1}{a^2} C_2. \end{cases} \tag{11}$$

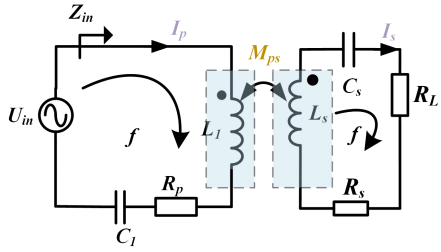

Fig. 14. Equivalent circuit diagram of the system working in single-frequency and single-load mode.

After the switch device is connected to the capacitor C_1, its equivalent value changes in the range of $[C_1, 10C_1]$; after the capacitor C_2 is connected to the switch device, its equivalent value changes in the range of $[C_2, 10C_2]$; after the inductance L_2 is connected to the switch device, its equivalent value changes in the range of $[L_2, 10L_2]$; according to (11), when the initial frequency is f_1, f_2, the two resonant frequency adjustment ranges are $[0.316f_1, f_1]$, $[0.316f_2, f_2]$, respectively.

$$\begin{bmatrix} U_{in} & 0 \end{bmatrix}^T = \begin{bmatrix} R_p + j\left(\omega L_1 - \frac{1}{\omega C_1}\right) & -j\omega M_{ps} \\ -j\omega M_{ps} & R_s + R_L + j\left(\omega L_s - \frac{1}{\omega C_s}\right) \end{bmatrix} \cdot \begin{bmatrix} I_p & I_s \end{bmatrix}^T \tag{12}$$

Combined with the analysis in Section III-A–E, the variable resonance network parameter design and adjustment mode are shown in Fig. 13.

As for Fig. 13, the parameters of the resonant network are initially determined according to the research in Section III-C. Then, based on the variation of load frequency, the variation values of each component parameter are determined. Then, the control angle of each switching device is designed according to the research in Section III-A–III-B. Finally, the equivalent values of each component are changed by the controller.

The dual-frequency mode is taken as an example to illustrate the adjustment mode of the variable resonant network. According to the values of the initial frequencies f_1, f_2 and the transmitting coil L_1 and (6), (7), the initial value of the resonant network is calculated. When the load frequency changes, the controller receives the target frequencies f_1'', f_2'', and the variation of each variable device can be calculated according to the changed frequencies f_1'', f_2'' and (9) and (11). The controller calculates the control angle of each variable device according to the variation sum, (3) and (4), and generates the corresponding control signal. The control signals control the corresponding MOSFET, respectively. The resonant frequency of the variable resonant network becomes the target value.

IV. Modeling and Characteristic Analysis of MFML WPT System Controlled by HM-PWM Based on Variable Resonant Network

In Section III, the variable resonance network is modeled and analyzed. In order to study the energy efficiency characteristics of the MFML WPT system controlled by HM-PWM based on the variable resonance network, the system needs to be modeled and analyzed. In the following, the energy efficiency characteristics of single-frequency and single-load and dual-frequency and dual-load WPT systems are researched.

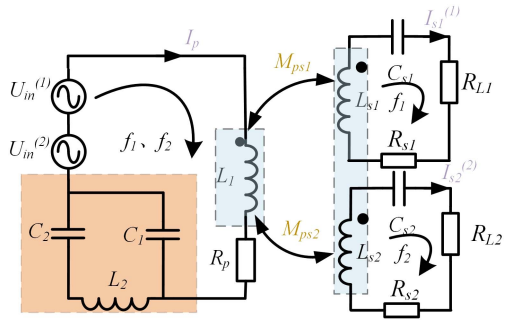

Fig. 15. Equivalent circuit diagram of the system.

A. Modeling and Characteristic Analysis of Single-Frequency and Single-Load WPT System

In order to analyze the energy efficiency characteristics, the model of the WPT system with single-frequency and single-load is analyzed. When the system works in single-frequency and single-load mode, the equivalent circuit of the system is shown in Fig. 14.

According to Kirchhoff's law, the voltage and current equations of the primary and secondary sides can be obtained in (12).

Since the system works at the resonant frequency, the parameters are satisfied [10]

$$\begin{cases} \omega L_1 = \frac{1}{\omega C_1} \\ \omega L_s = \frac{1}{\omega C_s} \end{cases}. \tag{13}$$

Therefore, the input impedance of the system can be obtained as

$$Z_{in} = R_p + \frac{(\omega M_{ps})^2}{R_s + R_L}. \tag{14}$$

At this point, the primary and secondary side currents I_p, I_s are

$$I_p = \frac{U_{in}}{Z_{in}} = \frac{(R_L + R_s)\, U_{in}^2}{R_p\,(R_L + R_s) + \omega^2 M_{ps}^2} \tag{15}$$

$$I_s = \frac{j\omega M_{ps} U_{in}}{R_p\,(R_L + R_s) + \omega^2 M_{ps}^2}. \tag{16}$$

Thus, the output power and transmission efficiency of the system can be solved as

$$P_{\mathrm{out}} = I_s^2 R_L \tag{17}$$

$$\eta_{st} = \frac{I_s^2 R_L}{I_s^2 R_L + I_p^2 R_p} \tag{18}$$

$$\begin{bmatrix} U_{in}^{(i)} & 0 & 0 \end{bmatrix}^T = \begin{bmatrix} Z_p^{(i)} & -j\omega_i M_{ps1} & -j\omega_i M_{ps2} \\ -j\omega_i M_{ps1} & Z_{s1}^{(i)} & 0 \\ -j\omega_i M_{ps2} & 0 & Z_{s2}^{(i)} \end{bmatrix}$$

TABLE I
PARAMETER TABLE OF THE SYSTEM OPERATING IN SINGLE-FREQUENCY AND SINGLE-LOAD MODE

Parameter	Symbol	Value		Parameter	Symbol	Value
Input voltage	U_d	40 V		Working frequency	f	30 kHz
Inductance of transmitter	L_1	136 uH	Case 1	Capacitor of Transmitter	C_1	207.07 nF
ESR of L_1	R_p	0.14 Ω		Capacitor of Receiver	C_s	120.53 nF
Inductance of receiver	L_s	233.5 uH		Working frequency	f'	20 kHz
ESR of Ls	Rs	0.2 Ω	Case 2	Capacitor of Transmitter	C_1'	465.73 nF
Mutual inductance	M_{ps}	33.63 uH		Capacitor of Receiver	C_s'	271.05 nF
Load	R_L	1 Ω	Distance of Transmitter to Receiver		D_{ps}	16 cm

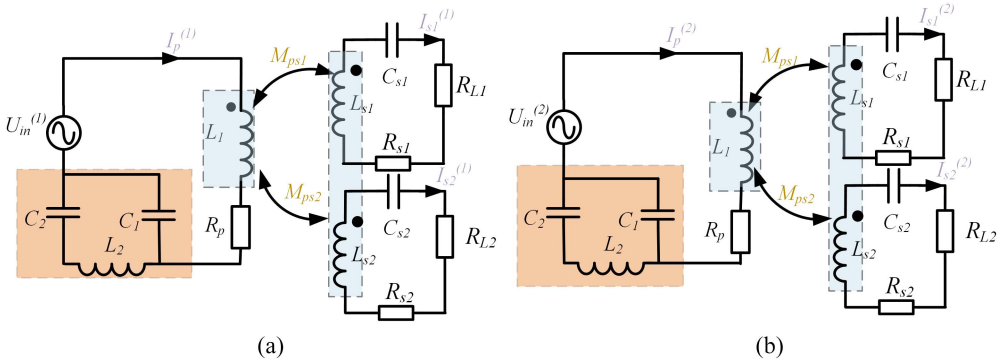

Fig. 16. Equivalent circuit diagram simplified by superposition principle. (a) $U_{in}^{(1)}$ acting alone. (b) $U_{in}^{(2)}$ acting alone.

$$\begin{bmatrix} I_p^{(i)} & I_{s1}^{(i)} & I_{s2}^{(i)} \end{bmatrix}^T. \tag{19}$$

In the case of single-frequency and single-load, the power factor of the system cosϕ=1, because the primary and secondary sides are resonant.

B. Modeling and Characteristic Analysis of Dual-Frequency and Dual-Load WPT System

In order to analyze the energy efficiency characteristics, the model of the dual-frequency and dual-load WPT system is analyzed. The equivalent circuit of the system working in dual-frequency and dual-load mode is shown in Fig. 15.

Based on the superposition principle, the circuit is shown in Fig. 15 can be equivalent to the circuit model is shown in Fig. 16.

According to Kirchhoff's voltage law, the voltage and current equations of the primary and secondary sides can be obtained in (19).

ω_i, $Z_p^{(i)}$, $Z_{s1}^{(i)}$, $Z_{s2}^{(i)}$ are, respectively, the angular frequency of the receiving loop, the input impedance of the transmitting and the receiving ends, which can be expressed as

$$\begin{cases} Z_p^{(i)} = R_p \\ Z_{s1}^{(i)} = R_{s1} + R_{L1} + j\left(\omega_i L_{s1} - \frac{1}{\omega_i C_{s1}}\right) \\ Z_{s2}^{(i)} = R_{s2} + R_{L2} + j\left(\omega_i L_{s2} - \frac{1}{\omega_i C_{s2}}\right) \end{cases} \tag{20}$$

where i = 1, 2 represents the two frequencies f_1 and f_2, respectively.

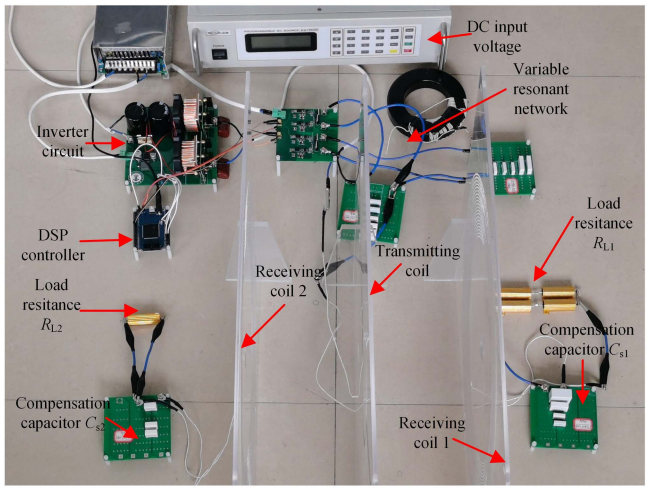

Fig. 17. Dual-frequency and dual-load WPT system experimental platform.

By combining (19) and (20), the primary current and secondary current can be obtained

$$\begin{cases} I_p^{(i)} = \frac{U_{in}^{(i)}}{Z_{in}^{(i)}} \\ I_{s1}^{(i)} = \frac{j\omega U_{in}^{(i)} M_{ps1}}{Z_{in}^{(i)} Z_{s1}^{(i)}} \\ I_{s2}^{(i)} = \frac{j\omega_i U_{in}^{(i)} M_{ps2}}{Z_{in}^{(i)} Z_{s2}^{(i)}} \end{cases}. \tag{21}$$

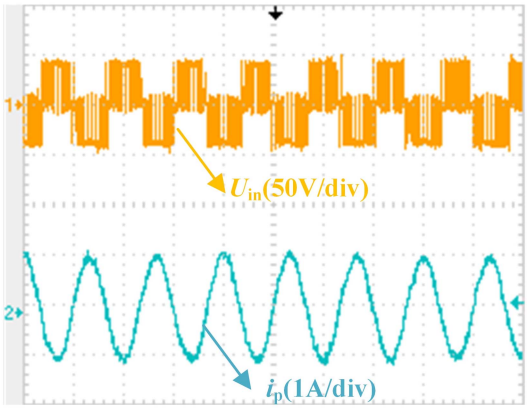

Fig. 18. Inverter output voltage and current waveforms at 30 kHz.

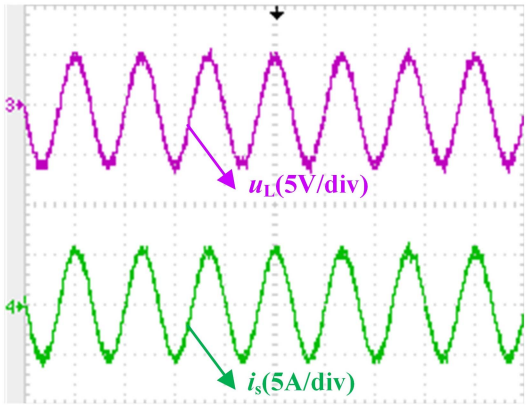

Fig. 19. Voltage and current waveforms of the secondary side load at 30 kHz.

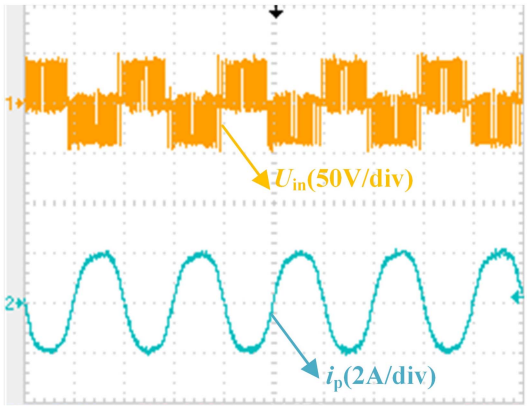

Fig. 20. Inverter output voltage and current waveforms at 20 kHz using a variable resonant network.

Because two modulated waves of different frequencies are combined to control the high-frequency inverter, the output voltage is equivalent to the superposition of the sinusoidal voltage of two different frequency bands. So, the power of each receiving circuit satisfies the superposition theorem. The output power of the two receiving loops are $P_{o1}^{(i)}$ and $P_{o2}^{(i)}$, the total output power of the two receiving loops are P_{o1} and P_{o2}. Based on the principle of superposition, it can be obtained that

$$\begin{cases} P_{o1}^{(i)} = \left|I_{s1}^{(i)}\right|^2 R_{L1} \\ P_{o2}^{(i)} = \left|I_{s2}^{(i)}\right|^2 R_{L2} \end{cases} \tag{22}$$

$$\begin{cases} P_{o1} = P_{o1}^{(1)} + P_{o1}^{(2)} \\ P_{o2} = P_{o2}^{(1)} + P_{o2}^{(2)}. \end{cases} \tag{23}$$

The loss of this system is mainly the internal resistance loss of the transmitting coil and the receiving coil. The power loss $P_{\text{loss}}^{(i)}$ for each frequency and the total power loss P_{loss} are

$$P_{\text{loss}}^{(i)} = \left(I_p^{(i)}\right)^2 R_p + \left(I_{s1}^{(i)}\right)^2 R_{s1} + \left(I_{s2}^{(i)}\right)^2 R_{s2} \tag{24}$$

$$P_{\text{loss}} = P_{\text{loss}}^{(1)} + P_{\text{loss}}^{(2)}. \tag{25}$$

The transmission efficiency from the transmitting end to the receiving end can be obtained as follows:

$$\eta = \frac{P_{\text{out}}}{P_{\text{out}} + P_{\text{loss}}} = \frac{P_{o1} + P_{o2}}{P_{o1} + P_{o2} + P_{\text{loss}}}. \tag{26}$$

In this mode, the system power factor is

$$PF = \frac{P}{\sqrt{P^2 + Q^2}} \tag{27}$$

where P is the total power of the system and Q is the reactive power of the system.

V. Experimental Verification

In order to verify the above analysis, the experimental platform of HM-PWM-controlled dual-frequency and dual-load WPT system based on variable resonant network is built. In order to ensure that the system can work normally under high-frequency conditions, GaN HEMT device is used to build the inverter, and DSPTMS320F28335 is used as the controller. The DSP generates control signals for the inverter and the SCC. The experimental platform is shown in Fig. 17.

A. Single-Frequency and Single-Load WPT System Controlled by HMW-PWM Based on Variable Resonant Network

The frequency switching experiment is carried out in single-frequency and single-load mode. The parameters of the experimental platform are shown in Table I.

When the resonant frequency of the receiving loop is 30 kHz, the waveforms of the inverter output voltage and current are shown in Fig. 18. The voltage and current waveforms of the secondary load are shown in Fig. 19.

According to Figs. 18 and 19, both the primary and secondary side currents are sinusoidal waves with a frequency of 30 kHz. It indicates that the system successfully receives 30 kHz electrical energy in the receiving loop under the condition of 30 kHz.

The resonant frequency of the receiving loop is adjusted to 20 kHz, one of the primary variable resonant network is changed to 20 kHz by DSP control, and the output frequency of the inverter is changed to 20 kHz. The output voltage and current

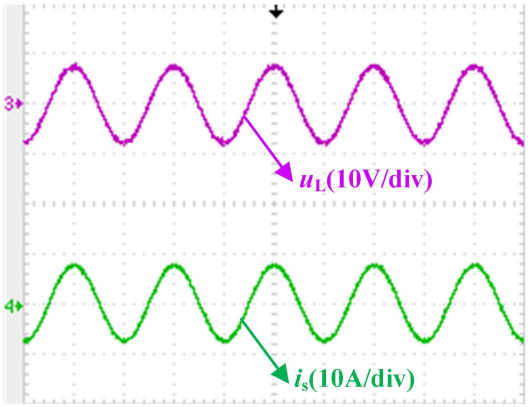

Fig. 21. Voltage and current waveforms of the secondary side load at 20 kHz using a variable resonant network.

TABLE II
EXPERIMENTAL RESULTS UNDER SINGLE-FREQUENCY AND SINGLE-LOAD MODE

	Case 1	Case 2	Replication case
Working frequency	30 kHz	20 kHz	20 kHz
Output power	15.68 W	28.837 W	32.83 W
Transmitter-to-receiver transmission efficiency	83.01%	82.56%	81.9%
Overall efficiency	71.5%	70.5%	61.36%
Power factor	0.99	0.99	0.432

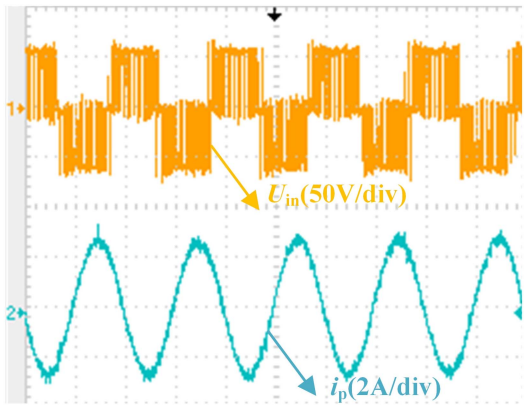

Fig. 22. Inverter output voltage and current waveforms at 20 kHz without compensation.

waveforms of the inverter are shown in Fig. 20, and the load voltage and current waveforms are shown in Fig. 21.

According to Figs. 20 and 21, both the primary and secondary currents are sinusoidal waves with a frequency of 20 kHz. Note The resonant frequency of the variable resonance network is switched from 30 to 20 kHz. The distortion caused by the primary side current is acceptable.

In order to further illustrate the compensation effect of variable resonance network, this article reproduced the experiment without compensation in [17] under the same circumstances. Under the condition of 20 kHz without a compensation network, the output voltage and current waveforms of the inverter are shown in Fig. 22, and the load voltage and current waveforms of the secondary side are shown in Fig. 23.

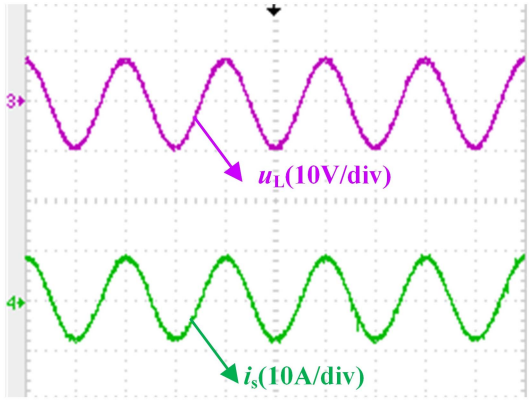

Fig. 23. Voltage and current waveforms of secondary side load at 20 kHz without compensation.

In order to make the system output power is the same without compensation and with compensation, the input voltage is increased to 59 V. By comparing Figs. 21 and 23, it can be seen that the output power of the two experimental systems is the same. According to Figs. 20 and 22, under the premise of the same output power, the current on the primary side of the network without compensation is larger. Meanwhile, the current on the primary side has a larger reactive power component, thus, the system has a larger reactive power. The variable resonant network can compensate the reactive power of the system when the inverter output frequency and load frequency change.

In addition, the efficiency of the system is

$$\eta_{\text{sys}} = \frac{P_{\text{out}}}{P_{\text{in}}} \tag{28}$$

where P_{out} is the total output power of the system, P_{in} is the total input power of the system.

According to Table II, the transmission efficiency and overall efficiency of case 1 and case 2 are basically unchanged before and after the frequency switching. And the power factor remains unchanged, indicating that the resonant frequency of the resonant network is switched from 30 to 20 kHz, and the output power is different due to the same experimental load and different frequencies, which is related to the impedance matching of the system. According to the analysis of case 2 and the repetition experiment, on the premise of the approximately same output power, although the frequency is flexible and adjustable without using the resonant network in [17], the system has large reactive power, low power factor, and low overall efficiency.

B. Dual-Frequency and Dual-Load WPT System Controlled by HMW-PWM Based on Variable Resonance Network

The frequency switching experiment was carried out under the condition of dual-frequency and dual-load, the experimental platform parameters are shown in Table III.

When the frequency of the two receiving loops is 30 and 90 kHz, the output voltage of the inverter is shown in Fig. 24, and the current of the two receiving loops is shown in Fig. 25

TABLE III
PARAMETER TABLE OF THE SYSTEM WORKING IN DUAL-FREQUENCY AND DUAL-LOAD MODE

Parameter	Symbol	Value		Parameter	Symbol	Value
Input voltage	U_d	100 V		Working frequency	f_1	30 kHz
Inductance of transmitter	L_1	136 uH			f_2	90 kHz
ESR of L_P	R_p	0.14Ω		Capacitor of Receiver-1	C_{s1}	120.52 nF
Inductance of Receiver-1	L_{s1}	233.5 uH	Case 1	Capacitor of Receiver-2	C_{s2}	13.39 nF
ESR of L_{s1}	R_{s1}	0.2Ω			L_2	555.33 uH
Inductance of Receiver-2	L_{s2}	233.28 uH		Resonant network	C_1	29.57 nF
ESR of L_{S2}	R_{s2}	0.2Ω			C_2	39.419 nF
Mutual inductance 1	M_{ps1}	31.495 uH		Working frequency	f_1''	20 kHz
Mutual inductance 2	M_{ps2}	30.2275 uH			f_2''	60 kHz
Load of Receiver-1	R_{L1}	1Ω		Capacitor of Receiver-1	C_{s1}	271.2 nF
Load of Receiver-2	R_{L2}	2Ω	Case 2	Capacitor of Receiver-2	C_{s2}	30.16 nF
Distance from transmitting coil to Receiver-1	D_{ps1}	16 cm			L_2''	555.33 uH
Distance from transmitting coil to Receiver-2	D_{ps1}	16 cm		Resonant network	C_1''	66.52 nF
					C_2''	88.79 nF

TABLE IV
EXPERIMENTAL RESULTS UNDER DUAL-FREQUENCY AND DUAL-LOAD MODE

	Case 1	Case 2	Replication case
Operating frequency	30 kHz 90 kHz	20 kHz 60 kHz	20 kHz 60 kHz
Output power	29.36 W	53.7 W	30.16 W
Transmitter-to-receiver transmission efficiency	84.66%	84.4%	84.77%
Overall system efficiency	70.91%	69.1%	62.12%
Power factor	0.99	0.99	0.62

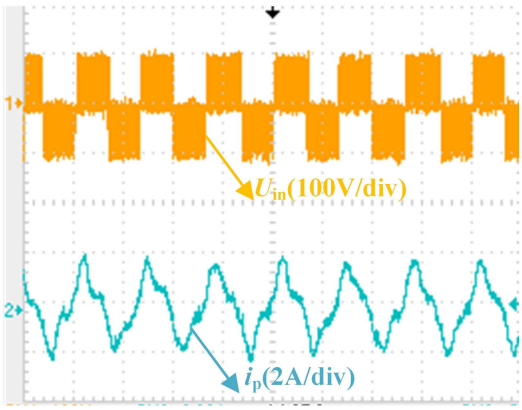

Fig. 24. Inverter output voltage and current waveforms at 30 and 90 kHz.

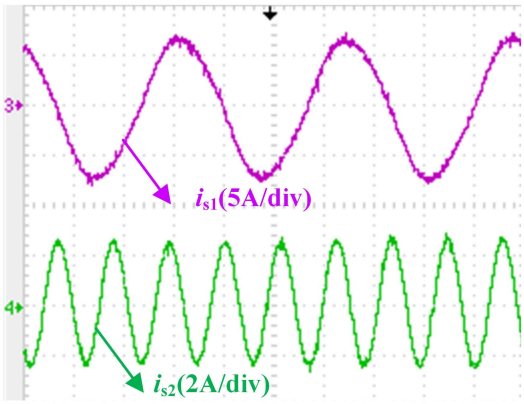

Fig. 25. Current waveforms of two receiving loops at 30 and 90 kHz.

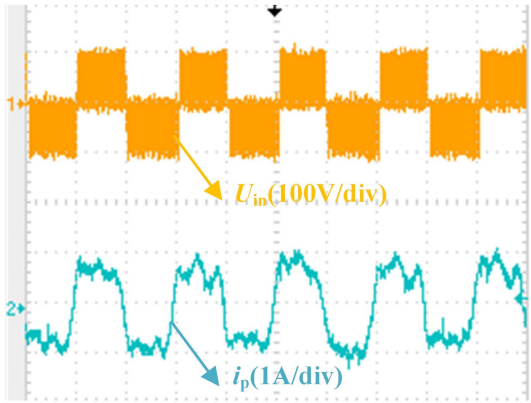

Fig. 26. Inverter output voltage and current waveform at 20 and 60 kHz using a variable resonant network.

According to Fig. 24, the output voltage of the inverter is a high-frequency hybrid pulse voltage, and the output current of the inverter is equivalent to the superposition of 30 and 90 kHz current. According to Fig. 25, the two receiving loops receive 30 and 90 kHz electrical energy, respectively.

The frequency of the two receiving loops is adjusted to 20 and 60 kHz, and the resonant frequency of the variable resonant network is changed to 20 and 60 kHz by DSP control. The output voltage and current waveforms of the inverter are shown in Fig. 26, and the current waveforms of the two receiving loops are shown in Fig. 27.

According to Fig. 26, the output voltage of the inverter is a high-frequency hybrid pulse voltage, and the output current of the inverter is equivalent to the superposition of 20 kHz current and 60 kHz current. The distortion of inverter output current due to the use of SCC is acceptable. According to Fig. 27, the two receiving loops receive 20 and 60 kHz electrical energy, respectively.

In order to further illustrate the compensation effect of variable resonant network, this article reproduced the experiment without compensation in [17] under the same circumstances. Under the condition of 20 and 60 kHz without compensation, the output voltage and current waveforms of the inverter are shown

TABLE V
PERFORMANCE COMPARISON

	Frequency adjustability	Transmission mechanism	Number of inverters	Efficiency(%)	Power factor
[10]	No	Simultaneous	Multiple	73–80	–
[11]	No	Simultaneous	Single	63.4	–
[17]	Yes	Simultaneous	Single	65–70	0.4–0.5
[19]	No	Time-sharing	Single	24–29	–
This work	Yes	Simultaneous	Single	71–72	0.99

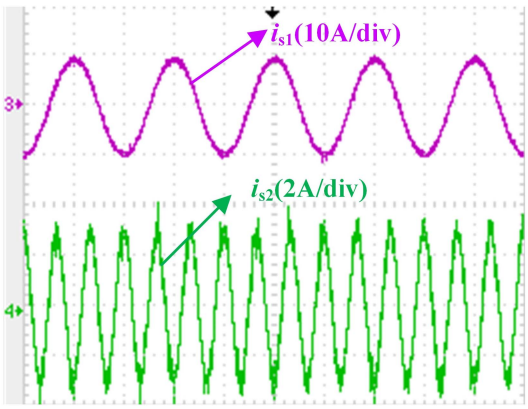

Fig. 27. Current waveforms of two receiving loops at 20 and 60 kHz using a variable resonant network.

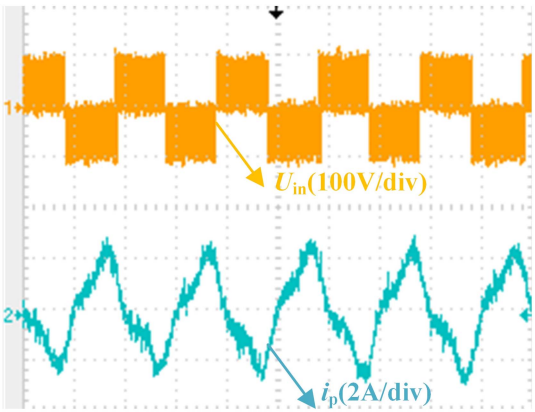

Fig. 28. 20 and 60 kHz inverter output voltage and current waveform without compensation.

in Fig. 28, and the current waveforms of the two receiving loops are shown in Fig. 29.

Comparing Figs. 27 and 29, it can be seen that the system output power is smaller without compensation. According to Figs. 26 and 28, under the premise of smaller system output power, the primary side current is larger without compensation, and there is a large reactive power in the system. The variable resonant network can compensate the reactive power of the system when the inverter output frequency and load frequency change. As shown in Table IV, the transmission efficiency and system efficiency of the case 1 and case 2 are basically unchanged before and after the frequency switching. The power factor also

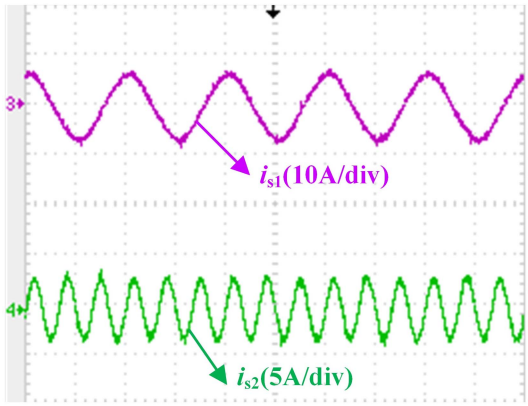

Fig. 29. 20 and 60 kHz current waveform of two receiving loops without compensation.

remains unchanged, indicating that the resonant frequency of the variable resonant network is switched from 30 and 90 kHz to 20 and 60 kHz. And the output power is different due to the same experimental load and different frequencies. According to case 2 and the repetition experiment, under the premise of the same input voltage, the output power of the system without using the resonant network in [17] is lower. And the system has larger reactive power, lower power factor, and lower system efficiency.

To illustrate the superior performance of the proposed variable resonant network in this article, Table V summarizes the performance of the proposed system in comparison to prior art.

As shown in Table V, the comparison has been carried out from the perspective of frequency adjustability, system performance, transmission mechanism, number of inverters, etc. In [10], multiple inverters are adopted to supply power for multiple loads with different frequencies simultaneously, and the efficiency reaches more than 70%. However, the cost of this system is high. In [10], [11], and [19], the frequencies of these systems are not continuously adjustable. In [19], the system uses a single inverter to supply power for loads with different frequencies and realizes independent control of multifrequency power. However, it cannot supply power for loads with different frequencies simultaneously and the system efficiency is low. In [17], although the frequency of the system is continuously adjustable, there is a problem of low power factor.

In this article, the proposed variable resonant network can flexibly change its resonant frequency, so that the system can flexibly supply power to loads with different frequencies. At the same time, the system keeps a high power factor.

VI. Conclusion

The innovation of this article is to put forward the idea of introducing variable elements into multifrequency resonant network to construct multifrequency variable resonant network. In order to verify the feasibility of this idea, an MFML MCR-WPT system controlled by the HM-PWM method based on variable resonant network and its control method are proposed. Taking dual-frequency and dual-load WPT system as an example, first, the parameter design method and control method of the variable resonant network are studied and realizing the change of resonant frequencies of single frequency and double frequencies resonant network. Second, the power and efficiency characteristics of single-frequency and single-load and dual-frequency and dual-load WPT systems are studied. Third, the power factor of the system is analyzed, so that the system always maintains a high power factor under the condition of frequency switching. Finally, the correctness of the theoretical analysis and the feasibility of the proposed method are verified by experiments. Through the analysis of the experimental results, compared with [17], the power factor of the variable resonant network proposed in this article has been greatly improved. Compared with the research of other researchers, this study not only keeps a high power factor, but also makes the resonant frequency of the system flexible and adjustable, thus reducing the cost.

However, this article still has the following shortcomings, which need to be further studied.

1) In order to realize the dynamic tuning of the resonant frequency of the resonant network, SCC and SCI are used in this article, so there is a certain loss. In the future, the structure and control method of switch controlled capacitor and inductance will be optimized to reduce their loss.
2) With the HM-PWM control method, the switching frequency of the inverter is high, thus, it is necessary to further improve the circuit topology or find new switching devices to reduce waveform distortion and achieve power transmission of higher frequency.

References

[1] Z. Zhang, H. Pang, A. Georgiadis, and C. Cecati, "Wireless power transfer–An overview," *IEEE Trans. Ind. Electron.*, vol. 66, no. 2, pp. 1044–1058, Feb. 2019.

[2] J. Dai and D. C. Ludois, "A survey of wireless power transfer and a critical comparison of inductive and capacitive coupling for small gap applications," *IEEE Trans. Power Electron.*, vol. 30, no. 11, pp. 6017–6029, Nov. 2015.

[3] C. Xia, R. Chen, Y. Liu, L. Liu, and G. Chen, "Inhibition of current harmonics in LCL/LCC wireless power transfer system," in *Proc. IEEE PELS Workshop Emerg. Technol.: Wireless Power Transfer*, 2017, pp. 1–6.

[4] C. Xia, W. Wang, S. Ren, X. Wu, and Y. Sun, "Robust control for inductively coupled power transfer systems with coil misalignment," *IEEE Trans. Power Electron.*, vol. 33, no. 9, pp. 8110–8122, Sep. 2018.

[5] Z. Yan, B. Song, Y. Zhang, K. Zhang, Z. Mao, and Y. Hu, "A rotation-free wireless power transfer system with stable output power and efficiency for autonomous underwater vehicles," *IEEE Trans. Power Electron.*, vol. 34, no. 5, pp. 4005–4008, May 2019.

[6] C. Zhang, N. Tang, W. Zhong, C. K. Lee, and R. S. Y. Hui, "A new energy harvesting and wireless power transfer system for smart grid," in *Proc. IEEE 7th Int. Symp. Power Electron. Distrib. Gener. Syst.*, 2016, pp. 1–5.

[7] Z. Huang, I. W. Iam, I. U. Hoi, C.-S. Lam, P.-I. Mak, and R. P. Martins, "Self-contained solar-powered inductive power transfer system for wireless electric vehicle charging," in *Proc. IEEE-PES Asia-Pacific Power Energy Eng. Conf.*, 2019, pp. 1–6.

[8] Z. Nie and Y. Yang, "A model independent scheme of adaptive focusing for wireless powering to in-body shifting medical device," *IEEE Trans. Antennas Propag.*, vol. 66, no. 3, pp. 1497–1506, Mar. 2018.

[9] H. Ju and R. Zhang, "Throughput maximization in wireless powered communication networks," *IEEE Trans. Wireless Commun.*, vol. 13, no. 1, pp. 418–428, Jan. 2014.

[10] F. Liu, Y. Yang, Z. Ding, X. Chen, and R. M. Kennel, "A multifrequency superposition methodology to achieve high efficiency and targeted power distribution for a multiload MCR WPT system," *IEEE Trans. Power Electron.*, vol. 33, no. 10, pp. 9005–9016, Oct. 2018.

[11] W. Liu, K. Chau, C. H. Lee, C. Jiang, W. Han, and W. Lam, "Multifrequency multi-power one-to-many wireless power transfer system," *IEEE Trans. Magn.*, vol. 55, no. 7, Jul. 2019, Art. no. 8001609.

[12] C. Qi, H. Miao, Z. Lang, and X. Chen, "A generalized methodology to generate, amplify and compensate multi-frequency power for a single-inverter-based MF-MR-S-WPT system," *IEEE Access*, vol. 8, pp. 181513–181525, 2020.

[13] Z. Han, F. Liu, and X. Chen, "Multi-frequency pulse width modulation control strategy for multi-load MCR WPT system with single transmitting coil," in *Proc. IEEE 9th Int. Power Electron. Motion Control Conf.*, 2020, pp. 741–746.

[14] W. Ye, X. Chen, and F. Liu, "Pulse density modulation control to achieve constant output voltage for multi-load magnetically coupled resonant wireless power transfer system," in *Proc. 10th Int. Conf. Power Electron., Mach. Drives*, 2020, pp. 222–229, doi: 10.1049/icp.2021.1009.

[15] E. Abramov and M. M. Peretz, "Multi-loop control for power transfer regulation in capacitive wireless systems by means of variable matching networks," *IEEE Trans. Emerg. Sel. Topics Power Electron.*, vol. 8, no. 3, pp. 2095–2110, Sep. 2020.

[16] R. Saltanovs, "Multi-capacitor circuit application for the wireless energy transmission system coils resonant frequency adjustment," in *Proc. IEEE Wireless Power Transfer Conf.*, 2015, pp. 1–3.

[17] C. Xia, N. Wei, H. Zhang, S. Zhao, Z. Li, and Z. Liao, "Multifrequency and multiload MCR-WPT system using hybrid modulation waves spwm control method," *IEEE Trans. Power Electron.*, vol. 36, no. 11, pp. 12400–12412, Nov. 2021.

[18] W.-J. Gu and K. Harada, "A new method to regulate resonant converters," *IEEE Trans. Power Electron.*, vol. 3, no. 4, pp. 430–439, Oct. 1988.

[19] X. Zhang, F. Liu, and T. Mei, "Multifrequency phase-shifted control for multiphase multiload MCR WPT system to achieve targeted power distribution and high misalignment tolerance," *IEEE Trans. Power Electron.*, vol. 36, no. 1, pp. 991–1003, Jan. 2021.

Chenyang Xia (Member, IEEE) was born in Jiangsu Province, China, in 1982. He received the B.S., M.S., and Ph.D. degrees in control theory and control engineering from Chongqing University, Chongqing, China, in 2006, 2008, and 2010, respectively.

From 2018 to 2019, he was an Academic Visitor with the University of Auckland, Auckland, New Zealand. He is currently a Professor with the School of Electrical Engineering, China University of Mining and Technology, Xuzhou, China. His research interests include wireless power transfer and intelligent control.

Yunhai Liu was born in Shandong Province, China, in 1998. He received the B.S. degree in electrical engineering from the China University of Mining and Technology, Jiangsu, China, in 2021.

His research interests include wireless power transfer and intelligent control.

Chenxu Wang was born in Anhui Province, China, in 2001. He received the B.S. degree in electrical engineering from the China University of Mining and Technology, Jiangsu, China, in 2023.

His research interests include wireless power transfer and intelligent control.

Zijian Yang received the B.S. degree in electrical engineering in 2021 from the China University of Mining and Technology, Xuzhou, China, where he is currently working toward the M.S. degree in electrical engineering with the School of Electrical Engineering.

His research interest includes wireless power transfer.

Gang Ren was born in Dalian City, Liaoning Province, China, in 1999. He received the bachelor's degree in electrical engineering and automation in 2021 from the China University of Mining and Technology, Xuzhou, China, where he is currently working toward the master's degree in electrical engineering.

His main research interests include wireless charging technology for electric vehicles and power electronic converter technology.

Jiaan Yan received the B.S. degree in electrical engineering in 2021 from the China University of Mining and Technology, Xuzhou, China, where he is currently working toward the M.S. degree in electrical engineering with the School of Electrical Engineering.

His research interest includes wireless power transfer.

Hao Lu received the B.S. degree in electrical engineering from Soochow University, Suzhou, China, in 2020. He is currently working toward the M.S. degree in electrical engineering with the School of Electrical Engineering, China University of Mining and Technology, Xuzhou, China.

His current research interest includes wireless power transfer.

Anran Sun received the B.S. degree in electrical engineering from Liaoning Technical University, Huludao, China, in 2019. He is currently working toward the Ph.D. degree in electrical engineering with the School of Electrical Engineering, China University of Mining and Technology, Xuzhou, China.

His research interest includes wireless power transfer.

Yang Lu was born in Zhoushan City, Zhejiang Province, China, in 1992. He received the B.Eng. degree in electrical engineering and automation from Southeast University, Nanjing, China, in 2015, and the M.Eng. degree in electrical engineering from Northeast Electric Power University, Jilin, China, in 2019. He is currently working toward the Ph.D. degree in electrical engineering with the China University of Mining and Technology, Xuzhou, China.

His main research interests include wireless power transmission, automated guided vehicle battery chargers, and technique of power electronics and power transmission, as well as photovoltaic energy storage.